



Research articles

Structures, magnetism and transport properties of the potential spin-gapless semiconductor CoFeMnSi alloy

Huarui Fu, Yunlong Li, Li Ma*, Caiyin You*, Qing Zhang, Na Tian

School of Materials Science & Engineering, Xi'an University of Technology, Xi'an 710048, PR China

ARTICLE INFO

Keywords:

Heusler alloy
Spin gapless semiconductor
Transport properties

ABSTRACT

The polycrystalline CoFeMnSi alloy with a potential spin gapless semiconductor (SGS) behavior was prepared by arc melting. The structures, magnetism and transport properties of CoFeMnSi alloy were investigated in detail. The occurrence of (1 1 1) superlattice XRD peak indicates the highly ordered Y-type structure of CoFeMnSi alloy. The saturation magnetization is around $3.49 \mu_B/\text{f.u.}$ and the Curie temperature is about 763 K. The transport properties exhibit a semiconducting-like behavior and the resistivity is about $269 \mu\Omega \text{ cm}$ at 300 K. The carrier concentration almost shows a non-dependence of temperature, which is different from that of traditional semiconductor, presenting a typical characteristic of spin gapless semiconductor. The carrier concentration and carrier mobility measured at 300 K are $4.9 \times 10^{20} \text{ cm}^{-3}$ and $46 \text{ cm}^2/\text{V.s.}$, respectively.

1. Introduction

Nowadays, Heusler-type spin gapless semiconductors (SGS) have received considerable interest in the fields of condensed matter physics and materials science due to their potential application in novel spintronic devices due to their specific band structure: top of the valence band and the bottom of the conduction band for the majority electrons touched at the Fermi level (E_F) with zero band gap, while a band gap observed for the minority electrons [1]. This special band structure of SGS can give rise to the following unique transport properties [2]: (1) the excitation of carriers with spin polarization of 100%; (2) no energy required to excite electrons from the valence band to the conduction band; (3) the completely separated polarized spin carriers based on Hall effect; (4) the ability to switch between spin-polarized carriers of *n*-type and *p*-type by applying a gate voltage; (5) carrier mobility is 2–4 times higher than that of conventional semiconductor because the modulation of the Fermi level could significantly change the concentration of spin-up and spin-down streams in the SGS; (6) the high sensitivity of SGS characteristics to external influences (e.g. temperature, electric field, stress, electromagnetic radiation and impurities), which are expected to be favorable to design the future spintronic devices [3].

Equiatomic quaternary Heusler compound CoFeMnSi alloy can be regarded as the intermediate product of Co_2MnSi [4] and Fe_2MnSi [5], which possess both half-metallic ferromagnetism and gapless semiconductor properties. CoFeMnSi alloy was originally considered to be a half-metallic ferromagnetic material [6–8] until its SGS behavior was

found and proved in the theoretical and experimental studies [9–11]. Moreover, CoFeMnSi alloy is expected to be one of the potential substitutes for diluted magnetic semiconductors owing to its high Curie temperature (T_C) [12]. In addition, CoFeMnSi alloy is useful for counteracting resistivity mismatch with conventional semiconductors [13]. But there are few works to investigate its phase transformation, microstructure and transport properties under the solidification process. In this paper, we fabricated the CoFeMnSi alloy by arc melting and comprehensively studied its essential attributes, including structures, magnetism and transport properties. The results provide an important experimental evidence for the potential application of CoFeMnSi alloy in spintronic devices.

2. Experimental

Polycrystalline CoFeMnSi alloy was prepared by arc melting appropriate quantities of various elements (the purity is higher than 99.9%). Additional 5 wt% manganese was added to compensate for evaporation loss. The structure of the samples was characterized by x-ray diffraction (XRD, Shimadzu Limited) with Cu K α radiation. The elemental composition was confirmed using scanning electron microscope (SEM, JEOL JSM-6700F). The high temperature magnetism was checked with vibrating sample magnetometer (VSM, 7035 model). The low temperature magnetism and transport measurements were performed within the temperature range of 5–300 K under an external magnetic field up to 30 kOe, using the Versa-lab comprehensive

* Corresponding authors.

E-mail addresses: shibihan@xaut.edu.cn (L. Ma), caiyinyou@xaut.edu.cn (C. You).<https://doi.org/10.1016/j.jmmm.2018.10.040>

Received 16 May 2018; Received in revised form 8 October 2018; Accepted 8 October 2018

Available online 09 October 2018

0304-8853/ © 2018 Elsevier B.V. All rights reserved.

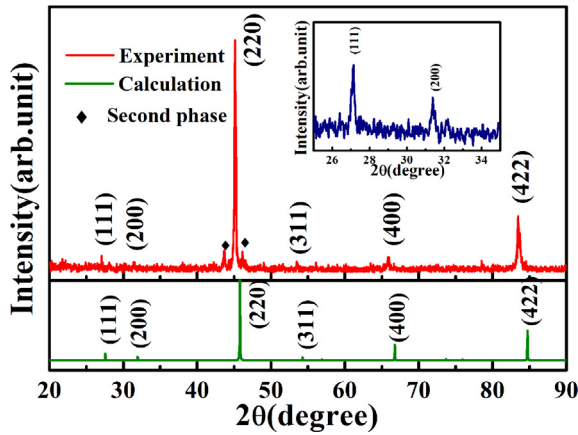


Fig. 1. Room-temperature X-ray diffraction pattern of CoFeMnSi compound and (inset) the expended part of the low angle region for XRD pattern.

physical analyzer (Quantum Design) and physical property measurement system (PPMS, Quantum Design PPMS-9).

3. Results and discussion

3.1. Structural properties

The ordering of Heusler alloys is directly related to the spin polarization, magnetism and transport properties [14]. Fig. 1 shows the room-temperature XRD pattern of CoFeMnSi alloy. It is reported from theoretical calculation that the LiMgPdSn-type equiatomic quaternary Heusler alloy CoFeMnSi is the highly ordered intermetallic compound with the prototype of Y-type structure (space group is $F\bar{4}3m$ (#216) with the atomic label $XX'YZ$) [10]. In the Wyckoff coordinate, the structure can be defined as four interpenetrating fcc lattice and the face centered structures are arranged in a diagonal order of $X-Y-X'-Z$ [10]. As seen from Fig. 1, the three typical diffraction peaks corresponding to CoFeMnSi (2 2 0), (4 0 0) and (4 2 2) can be observed, which indicate the polycrystalline structure of CoFeMnSi. From the expanded XRD pattern of the low angle region, as shown in the inset of Fig. 1, the diffraction peak of (1 1 1) can be observed, indicating the formation of highly ordered Y-type structure of CoFeMnSi [7]. To further estimate the chemical order of CoFeMnSi, we calculated the intensity ratios of I_{200}/I_{220} and I_{111}/I_{220} . It is reported that the superlattice reflections (2 0 0) and (1 1 1) are proportional to the chemical ordering factors defined as S^2 and $S^2(1-2\alpha)^2$, respectively [15]. And the two ordering factors can be described as:

$$S^2 = (I_{200}/I_{220})_{Exp.}/(I_{200}/I_{220})_{Theory} \quad (1)$$

$$S^2(1-2\alpha)^2 = (I_{111}/I_{220})_{Exp.}/(I_{111}/I_{220})_{Theory} \quad (2)$$

The $S = 0$ & $\alpha = 0$ and $S = 1$ & $\alpha = 0.5$ denote the disordered $A2$ structure and ordered $B2$ structure, respectively. The $S = 1$ and $\alpha = 0$ corresponds to the well-ordered cubic structure [7,15]. With respect to the XRD analyses, we calculated the $S = 1$ and $\alpha = 0$, demonstrating the CoFeMnSi in our work exhibiting a well-ordered cubic Heusler structure (LiMgPdSn-type or Y-type structure) [7]. In addition, the lattice constant of CoFeMnSi is 5.67 Å, which is 1.23% larger than the theoretical value (5.601 Å) [6].

The micro-morphology of the CoFeMnSi alloy is observed by SEM. As shows in Fig. 2(a), it is clear to see that there are three different regions (A, B and C regions) in the sample, implying that there exist three different phases in CoFeMnSi alloy. The average atomic concentrations as recorded by energy dispersive spectrum (EDS) spectroscopy for the A, B and C regions were $Co_{0.90}Fe_{0.95}Mn_{0.96}Si_1$, $Co_{0.99}Fe_{1.11}Mn_{1.59}Si_1$ and $Co_{0.81}Fe_{0.66}Mn_{1.21}Si_1$, respectively. According to the elemental mapping measurement (as shows in Fig. 2(b)),

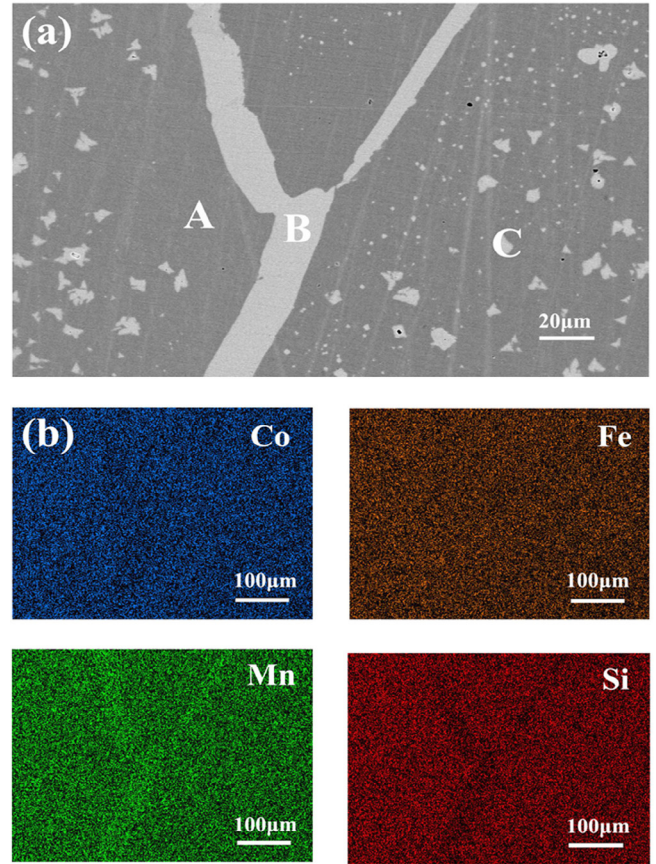


Fig. 2. (a) SEM image of the CoFeMnSi alloy at room temperature and (b) the elemental mappings of Co, Fe, Mn, Si, respectively.

the B, and C regions are Mn-rich phase, which could be corresponding to the impurity peaks in XRD pattern.

3.2. Magnetic properties

Fig. 3(a) shows the typical magnetic hysteresis loops measured at different temperatures for CoFeMnSi alloy. The inset of Fig. 3(a) presents the curve around the zero field for the measurement at 300 K. The sample is magnetically soft with extremely small coercivity as shown in the inset of Fig. 3(a). The saturation magnetization M_s is 98.6 emu/g ($3.49 \mu_B/f.u.$) and smaller than the value of $4 \mu_B/f.u.$ (mainly contributed by Mn atoms) based on the Slater-Pauling (SP) rule [12]. The discrepancy between experimental M_s value and the saturation moment predicated by SP rule is probably ascribed to the factors of presence of chemical disordered structures and impurities [12]. According to the XRD and EDS characterizations, the second phases, disordered structures and composition deviation of main phase can be observed in CoFeMnSi, which could give rise to non-integer position occupation or atomic site disorder. The dislocation of the Mn atoms could easily occur when Mn atoms and the neighboring Co or Fe atoms swapped or fell into tetrahedral space, leading to the decrease of total magnetic moment [8].

Fig. 3(b) shows the dependence of the spontaneous saturation magnetization (M_s) of the CoFeMnSi alloy on the temperature (T) and the inset is thermal magnetic curve. The curve can be well fitted by:

$$M_s(T) = cT^a + b \quad (3)$$

Here $a = 1.55$ and $M_s(T)$ approximately follows the Bloch formula [16]:

$$M_s(T) = M_s(0)(1 - kT^{1.5}) \quad (4)$$

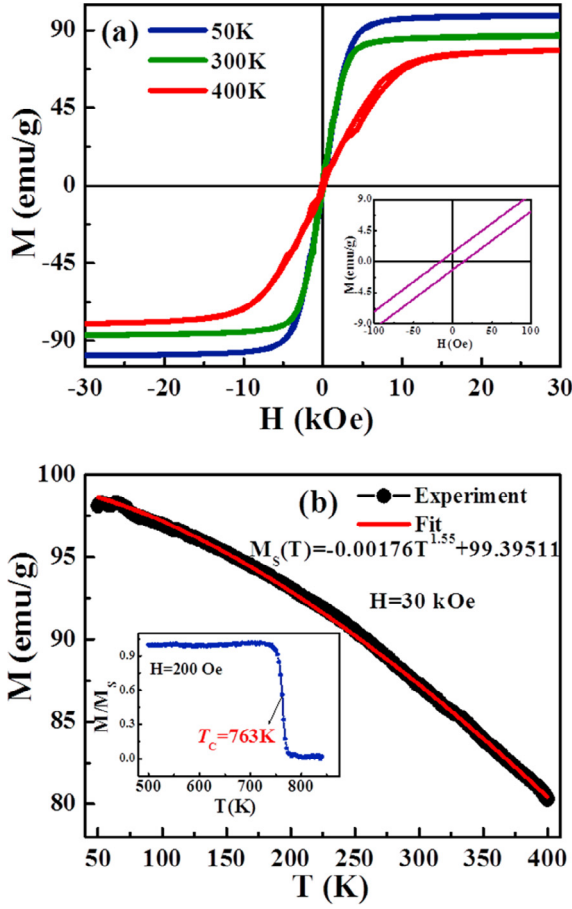


Fig. 3. (a) Magnetic hysteresis loops measured at different temperatures and (inset) the enlarged view of M-H loops for a better guide of eye to observe its coercivity; (b) the dependence of saturation magnetization (M_s) on temperature (T) and (inset) the thermal magnetic curve.

The thermal magnetic curve is shown in inset of Fig. 3(b), the single-phase magnetic transition can be observed and the Curie temperature is 763 K for the CoFeMnSi alloy, which is 140 K higher than the values reported by L. Bainsla et al. [10]. From the SEM and EDS characterizations, we observed obvious image contrast between main phase (region A) and Mn-rich area (regions B and C) in CoFeMnSi (as shown in Fig. 2(a)). The composition of the main phase is around $\text{Co}_{24}\text{Fe}_{25}\text{Mn}_{25}\text{Si}_{26}$, which deviated from the stoichiometric ratio and exhibited the Si-rich CoFeMnSi. Relevant paper reported that the T_c increases with increasing the Si content in Heusler alloy $\text{Co}_2\text{MnAl}_{1-x}\text{Si}_x$ [17] and $\text{Co}_2\text{FeAl}_{1-x}\text{Si}_x$ [18]. Moreover, the T_c is closely related to the chemical ordering structure of Heusler alloys, presenting a higher value of B2-type structure than that of $L2_1$ -type structure due to the increased interchange energy between transition metal atoms and main group atoms [17]. Thus, the Si-rich concentration and the partial B2 structures caused the increased Curie temperature of CoFeMnSi. The higher Curie temperature is more favorable for its applications in spintronic devices.

3.3. Transport characteristics

Fig. 4(a) shows the temperature dependence of the longitudinal conductivity (σ_{xx}) and the longitudinal resistivity (ρ_{xx}) (the inset of Fig. 4(a)) of CoFeMnSi alloy. It can be seen that the conductivity increases with increasing temperature, indicating the semiconducting-like behavior of CoFeMnSi alloy [10,19]. The σ_{xx} value is about 3712 S/cm at a temperature of 300 K, which is larger than the value of 2980 S/cm in the bulk SGS of CoFeMnSi [10] and is in the same order of magnitude with that in other Heusler SGSs including CoFeCrAl (4545 S/

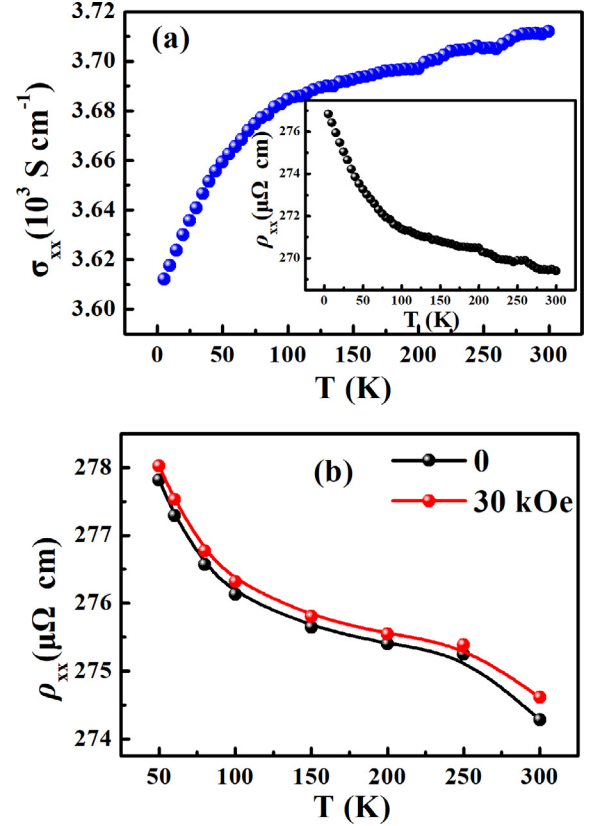


Fig. 4. (a) The temperature dependence of the longitudinal conductivity (σ_{xx}) and longitudinal resistivity (ρ_{xx}) (inset); (b) the longitudinal resistivity as a function of temperature measured at the magnetic field of 0 and 30 kOe, respectively.

cm) [13], bulk Fe_2CoSi (3333 S/cm) [5], and Mn_2CoAl film (3571 S/cm) [20]. The differences of the σ_{xx} value are mostly ascribed to the second phases, structural disorder and composition deviation of CoFeMnSi [10,19,20]. As seen in the inset of Fig. 4(a), the ρ_{xx} is 269 $\mu\Omega$ cm of CoFeMnSi at room temperature without magnetic field, which is close to the theoretical value (maximum value around at 250 $\mu\Omega$ cm) calculated by J. Kudrnovsky et al. through estimating corresponding formation energies of possible swap defects [21]. They found that the ρ_{xx} is varied with the Co-Fe swap defects, which determine the competitive factors between the scattering rate of electrons and the value of the DOS at E_F [21]. The larger ρ_{xx} value in our system could be due to the presence of structural defects during experimental preparation. Fig. 4(b) shows the temperature dependence of the longitudinal resistivity (ρ_{xx}) of CoFeMnSi alloy at $H = 0$ and $H = 30$ kOe. It can be seen that the longitudinal resistivity increases when the magnetic field is 30 kOe, indicating that the positive magnetoresistance effect for CoFeMnSi alloy. The magnetic resistance (MR) is 0.074% at 50 K, defined as:

$$MR = (\rho_H - \rho_0) / \rho_0 \quad (5)$$

Fig. 5(a) is the typical Hall loops of the CoFeMnSi alloy sample measured at various temperatures. The Hall loop shows the similar shape of the hysteresis loop because the anomalous Hall effect is closely related to the magnetism of the material. The total Hall resistivity of ferromagnetic materials can be expressed as:

$$\rho_{xy} = R_0 H_z + R_s M_z \quad (6)$$

with R_0 the ordinary Hall coefficient, H_z the component of the external magnetic field perpendicular to the surface of the sample, R_s the anomalous Hall coefficient. The first term represents the contribution of the ordinary Hall effect, and the second term represents the

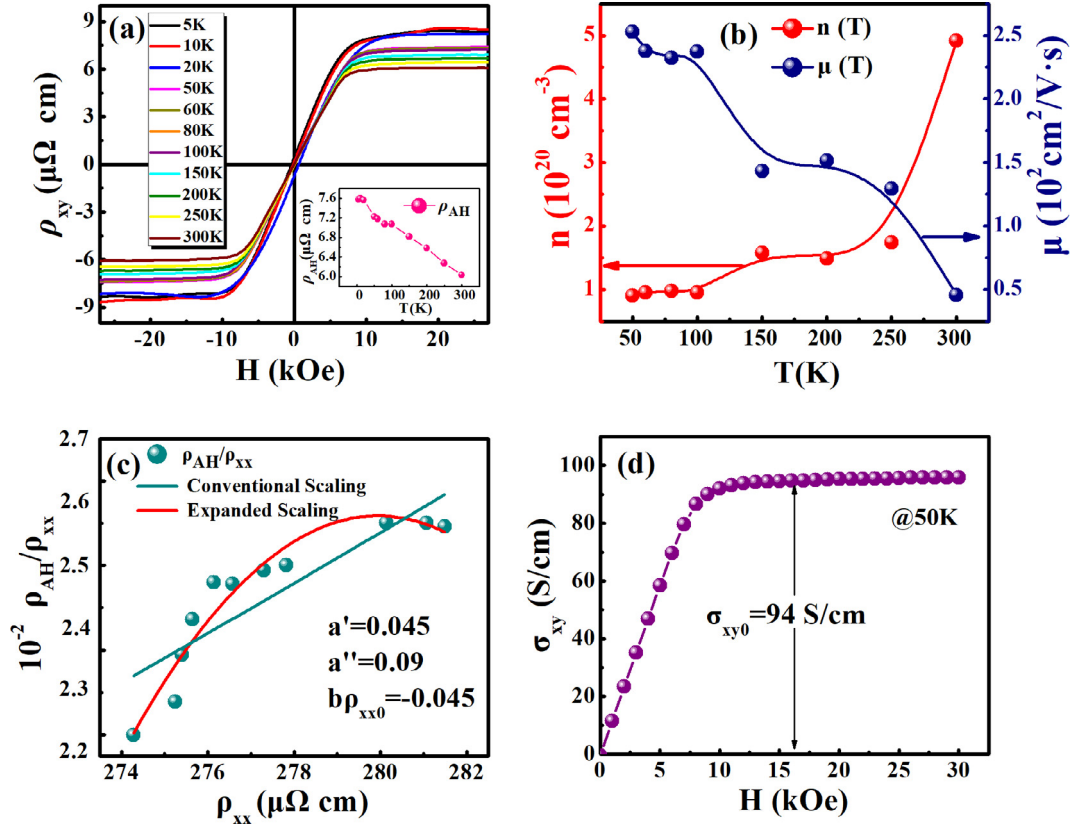


Fig. 5. (a) The typical Hall curves, the inset shows the relation of the anomalous Hall resistivity with temperature; (b) the relationship of carrier concentration (red) and carrier mobility (blue) with temperature; (c) the scale relation between Hall angle and longitudinal resistivity; (d) anomalous Hall conductivity varies with the magnetic field.

contribution of the anomalous Hall effect. The anomalous Hall resistivity was obtained by extrapolating the Hall resistivity at high fields to zero field. The inset shows that the anomalous Hall resistivity decreases linearly with temperature. According to the linear slope of Hall resistivity at high fields, the ordinary Hall coefficient R_0 is calculated as positive, indicating that CoFeMnSi alloy is p-type semiconductor. Both carrier concentration n (T) and carrier mobility μ (T) can be calculated from R_0 by

$$n(T) = 1/eR_0 \quad (7)$$

$$\mu(T) = R_0/\rho_{xx} \quad (8)$$

The result is shown in Fig. 5(b), the carrier concentration almost remains constant within the temperature range of 50–250 K, which is different from that of traditional semiconductor, presenting a typical characteristic of spin gapless semiconductor. The carrier concentration is $4.9 \times 10^{20} \text{ cm}^{-3}$ at 300 K, which is one order of magnitude smaller than that of the half-metallic Fe_2VAl (10^{21} cm^{-3}) [22] and much larger than that of the bulk Mn_2CoAl (10^{17} cm^{-3}) [23]. The carrier mobility decreases with increasing temperature, and reaches $46 \text{ cm}^2/\text{V}\cdot\text{s}$ at 300 K.

Based on the traditional scaling law, the anomalous Hall effect can be expressed as:

$$\rho_{AH} = a\rho_{xx} + b\rho_{xx}^2 \quad (9)$$

the fitting parameters a and b represent the contribution of skew scattering and the total contribution of intrinsic mechanism and side jump [24], respectively. Generally, the Hall angle (ρ_{AH}/ρ_{xx}) and longitudinal resistivity (ρ_{xx}) satisfy linear relations as shown with the green lines in Fig. 5(c). However, the Hall angle of the CoFeMnSi alloy deviates significantly from the linear scale relation, which meets the new scaling law [25]:

$$\rho_{AH} = a'\rho_{xx0} + a''\rho_{xxT} + b\rho_{xx}^2 \quad (10)$$

where ρ_{xx0} is the residual resistivity arising from the scattering of impurities and here we noted the ρ_{xx0} value by extrapolating the ρ_{xx} - T curve (see the inset of Fig. 4 (a)) to zero temperature, and ρ_{xxT} (defined as $\rho_{xxT} = \rho_{xx} - \rho_{xx0}$) is the phonon-induced resistivity. The parameters of a' , a'' and b are related to the contributions from impurity induced skew scattering, phonon induced skew scattering and Berry curvatures, respectively. The scaling results suggest that the AHE of CoFeMnSi film originates from both intrinsic and extrinsic contributions. Moreover, the second term (a'') is larger than the intrinsic contribution ($b\rho_{xx0}$), indicating that the contribution of phonon-related skew scattering is non-negligible [26,27], which mainly originates from the phonon-carrier (holes) interaction. This tendency is consistent with the Heusler SGS Mn_2CoAl system [27]. The anomalous Hall conductivity σ_{xy} can be obtained by:

$$\sigma_{xy} = \rho_{xy}/\rho_{xx}^2 \quad (11)$$

As shown in Fig. 5(d), the anomalous Hall conductivity (94 S/cm) of CoFeMnSi alloy is larger than that of the bulk Mn_2CoAl (22 S/cm) [23] but lower than that of the bulk CoFeCrGa (185 S/cm) [28].

4. Conclusions

CoFeMnSi alloy with the highly ordered Y-type structure was fabricated by arc melting, which exhibits a saturation magnetization of $3.49 \mu_B/\text{f.u.}$ and the Curie temperature of 763 K. Its transport properties exhibit a semiconducting-like behavior with a room temperature resistivity of $269 \mu\Omega \text{ cm}$. The carrier concentration and carrier mobility at 300 K are $4.9 \times 10^{20} \text{ cm}^{-3}$ and $46 \text{ cm}^2/\text{V}\cdot\text{s}$, respectively. The nonlinear scaling relationship between Hall angle and longitudinal resistivity was found through investigating the anomalous Hall effect of bulk sample.

These characteristics of CoFeMnSi alloy show its promising application for new spintronic devices.

Acknowledgments

This work was in part supported by the National Natural Science Foundation of China (Nos. 51771145, 51171148), Shaanxi key R & D plan, international scientific and technological cooperation and exchange program (No. 2017KW-020), Shaanxi Natural Science Basic Research Plan (Nos. 2017JM5060, 2018JQ1066).

Appendix A. Supplementary data

Supplementary data to this article can be found online at <https://doi.org/10.1016/j.jmmm.2018.10.040>.

References

- [1] X.T. Wang, Z.X. Cheng, J. Wang, X.L. Wang, G.D. Liu, J. Mater. Chem. C 4 (2016) 7176–7198.
- [2] X.L. Wang, Phys. Rev. Lett. 100 (2008) 156404.
- [3] K. Ueda, S. Hirose, H. Asano, Appl. Phys. Lett. 110 (2017) 202405.
- [4] H.R. Fu, C.Y. You, Y.L. Li, K. Wang, N. Tian, J. Phys. D: Appl. Phys. 49 (2016) 195001.
- [5] Y. Du, G.Z. Xu, X.M. Zhang, Z.Y. Liu, S.Y. Yu, E.K. Liu, W.H. Wang, G.H. Wu, Europhys. Lett. 103 (2013) 37011.
- [6] X.F. Dai, G.D. Liu, G.H. Fecher, C. Felser, Y.X. Li, H.Y. Liu, J. Appl. Phys. 105 (2009) 07E901.
- [7] V. Alijani, S. Ouardi, G.H. Fecher, J. Winterlik, S.S. Naghavi, X. Kozina, G. Stryanyuk, C. Felser, E. Ikenaga, Y. Yamashita, S. Ueda, K. Kobayashi, Phys. Rev. B 84 (2011) 224416.
- [8] H. Bhatt, M.D. Mukadam, S.S. Meena, S.M. Yusuf, AIP Conf. Proc. 1665 (2015) 130048.
- [9] G.Z. Xu, E.K. Liu, Y. Du, G.J. Li, G.D. Liu, W.H. Wang, G.H. Wu, Europhys. Lett. 102 (2013) 17007.
- [10] L. Bainsla, A.I. Mallick, M.M. Raja, A.K. Nigam, B.S.D.Ch.S. Varaprasad, Y.K. Takahashi, A. Alam, K.G. Suresh, K. Hono, Phys. Rev. B 91 (2015) 104408.
- [11] V.K. Kushwaha, J. Rani, A. Tulapurkar, C.V. Tomy, Appl. Phys. Lett. 111 (2017) 152407.
- [12] K. Özdoğan, E. Şaşıoğlu, I. Galanakis, J. Appl. Phys. 113 (2013) 193903.
- [13] P. Kharel, W. Zhang, R. Skomski, S. Valloppilly, Y. Huh, R. Fuglsby, S. Gilbert, D.J. Sellmyer, J. Phys. D: Appl. Phys. 48 (2015) 245002.
- [14] R. Shan, H. Sukegawa, W.H. Wang, M. Kodzuka, T. Furubayashi, T. Ohkubo, S. Mitani, K. Inomata, K. Hono, Phys. Rev. Lett. 102 (2009) 246601.
- [15] P.J. Webster, K.R.A. Ziebeck, J. Phys. Chem. Solids 34 (1973) 1647–1654.
- [16] K.R. Kumar, N.H. Kumar, G. Markandeyulu, J.A. Chelvane, V. Neuc, P.D. Babu, J. Magn. Magn. Mater. 320 (2008) 2737–2740.
- [17] R.Y. Umetsu, K. Kobayashi, A. Fujita, R. Kainuma, K. Ishida, Scr. Mater. 58 (9) (2008) 723–726.
- [18] H.F. Gerhard, F. Claudia, J. Phys. D: Appl. Phys. 40 (6) (2007) 1582.
- [19] H.R. Fu, C.Y. You, F.Q. Xin, L. Ma, N. Tian, Appl. Phys. Lett. 112 (26) (2018) 262406.
- [20] M.E. Jamer, B.A. Assaf, T. Devakul, D. Heiman, Appl. Phys. Lett. 103 (2013) 142403.
- [21] J. Kudrnovský, V. Drchal, S.K. Bose, I. Turek, Phys. Rev. B 97 (2018) 214404.
- [22] V.I. Okulov, V.E. Arkhipov, T.E. Govorkova, A.V. Korolev, K.A. Okulova, Low. Temp. Phys. 33 (2007) 692.
- [23] S. Ouardi, G.H. Fecher, C. Felser, J. Kubler, Phys. Rev. Lett. 110 (2013) 100401.
- [24] L. Berger, Phys. Rev. B 2 (1970) 4559.
- [25] Y. Tian, L. Ye, X. Jin, Phys. Rev. Lett. 103 (2009) 087206.
- [26] N.Y. Sun, Y.Q. Zhang, W.R. Che, R. Shan, Z.G. Zhu, J. Magn. Magn. Mater. 405 (2016) 311–316.
- [27] N.Y. Sun, Y.Q. Zhang, H.R. Fu, W.R. Che, C.Y. You, R. Shan, AIP. Adv. 6 (2016) 015006.
- [28] L. Bainsla, A.I. Mallick, M.M. Raja, A.A. Coelho, A.K. Nigam, D.D. Johnson, A. Alam, K.G. Suresh, Phys. Rev. B 92 (2015) 045201.